Materials Research Bulletin 172 (2024) 112670

Contents lists available at ScienceDirect

Materials Research Bulletin

journal homepage: www.elsevier.com/locate/matresbu

Research Papers

Design of morphology-controlled cobalt-based spinel oxides for efficient X-band microwave absorption

Yun Han [a,1], Mengjun Han [a,1], Tianbao Zhao [a,b,1], Zihao Xia [a], Jiaxiao Zou [a], Xuehua Liu [b,*], Zirui Jia [a,b,*]

[a] College of Chemistry and Chemical Engineering, Qingdao University, Qingdao, Shandong 266071, PR China
[b] State Key Laboratory of Bio-fibers and Eco-textiles, College of Materials Science and Engineering, Institute of Materials for Energy and Environment, Qingdao University, Qingdao 266071, PR China

ARTICLE INFO

Keywords:
$MnCo_2O_{4.5}$
Spinel crystalline
Nanostructure design
Electromagnetic wave absorption

ABSTRACT

The cobalt-based spinel structure oxides with synergistic effect of magnetic loss and dielectric loss have important applications in electromagnetic wave absorption. And the excess 0.5 oxygen atoms in $MnCo_2O_{4.5}$ provide more vacancies than traditional $MnCo_2O_4$ spinel structure and improve the electrical conductivity. In the current study, $MnCo_2O_{4.5}$ microsphere clusters, $MnCo_2O_{4.5}$ microcubic spheres and $MnCo_2O_{4.5}$ flowery spheres were prepared by solvothermal method and annealing process. Among the final samples with different morphologies, $MnCo_2O_{4.5}$ microcubic spheres showed outstanding microwave absorption capabilities, with a minimum reflection loss (RL_{min}) of -51.52 dB at 2.2 mm. When the thickness was further increased to 2.3 mm, the effective absorption bandwidth could be as wide as 5.36 GHz, covering most of the X-band. The excellent absorption performance of electromagnetic waves is related to the modulability of the complex dielectric parameters, the optimization of impedance matching, and the enhancement of the polarization relaxation process through the improvement of the morphologies. This work provides guidance and support for refining the electromagnetic wave absorption potential of cobalt-based spinel oxides and for designing highly efficient electromagnetic wave absorbers in the X-band.

1. Introduction

There is increasing concern that electromagnetic wave (EMW) have caused harm to human life and machine operation in society nowadays. The upgrading of electronic products sought after by most young people, leading to that the EMW pollution is also gaining [1–3]. Developing efficient absorbing materials to reduce electromagnetic radiation pollution is of significance, thus EMW absorption have become a hot spot for researchers [4–7].

AB_2O_4 spinel material is researched widely due to its high magnetism and excellent electronic properties, and is an ideal material for exploring the field of EMW absoption. The crystal lattice of spinel is a face-centered cubic tightly packed, AB_2O_4, type belongs to the cubic crystal system [8–13]. A and B represent divalent and trivalent metal cations, in tetrahedral and octahedral interstitial spaces in the crystal lattice. And they can be replaced by other elements in different oxidation states, forming structural defects. Thus far, plenty of EMW absorbers which have the same strutures with ACo_2O_4 (A=Co, Zn, Mn et al.) have been made and it got excellent marks. Recently investigators have examined the effects of absorption performance based on ACo_2O_4. By changing the calcination temperature, Wang et al. investigated to illuminate the $ZnCo_2O_4$ has the minimum reflection loss (RL_{min}) of −43.61 dB at 2.4 mm, and the effective absorption bandwidth (EAB) is 7.12 GHz at 2.8 mm [14–17]. This research seek to examine the effect of conductivity loss and multiple reflection due to the different microstrutures in EMW absorption. Zhou et al. put forward that the RL_{min} of $NiCo_2O_4$ is −44.5 dB at 5.3 mm, and the its EAB is calculated as 4.48 GHz at 5.1 mm. After that, they prepared $NiCo_2{\times}4$ (X=S, Se, Te) successfully. Among these metal oxide materials, the cobalt spinel structure oxides had been researched deeply, which are outstanding EMW absorbers due to their low price and high electrical conductivity. However, $MnCo_2O_{4.5}$ with unique surface structure has rarely been reported as a study of

* Corresponding authors at: State Key Laboratory of Bio-fibers and Eco-textiles, College of Materials Science and Engineering, Institute of Materials for Energy and Environment, Qingdao University, Qingdao 266071, PR China.
E-mail addresses: liuxuehua@qdu.edu.cn (X. Liu), jiazirui@qdu.edu.cn (Z. Jia).
[1] Contributed equally to this work.

https://doi.org/10.1016/j.materresbull.2023.112670
Received 25 November 2023; Received in revised form 21 December 2023; Accepted 30 December 2023
Available online 31 December 2023

microwave absorbing materials. Li et al. found that $MnCo_2O_4$ and $MnCo_2O_{4.5}/Co_2NiO_4$ had the RL_{min} of −43 dB and −40.01 dB at 2.4 mm and 2.00 mm, respectively. By changing the corresponding solvents and hydrothermal temperatures/time, the microstrutures of $MnCo_2O_{4.5}$ can be changed, and the competence in EMW absorption of the materials can be effectively improved [18–23]. Furthermore, the additional oxygen elemets in $MnCo_2O_{4.5}$ creates vacant void than traditional spinel structures of AB_2O_4 and helps to improve electrical conductivity. This work provides guidance and support for refining the EMW absorption potential of cobalt-based spinel oxides and for designing highly efficient EMW absorbers in the X-band. Thus $MnCo_2O_{4.5}$ nanomaterials had become proposal materials in the field of EMW absorption.

The different morphologies of the same material will produce various effects in the aspect of EMW absorption [24–26]. $NiCo_2O_4$ with multiple morphologies is researched widely for absorbing EMW. Li et al. propitiously manufactured $NiCo_2O_4$ with distictive morphologies by transforming dissolvants and medicines during the experinences. The bayberry-like $NiCo_2O_4$ obtains an RL_{min} value of −39 dB and its absorbing bandwidth is 3.1 GHz in 2.5 mm [27]. The RL_{min} of needle array clusters $NiCo_2O_4$ is −45 dB. The urchin-like $NiCo_2O_4$ with dielectric loss ability has a RL_{min} value of −40 dB at 1.4 mm, and its EAB is 4 GHz [28]. The sheet-like $NiCo_2O_4$ and hollow spheres like $NiCo_2O_4$ have the RL_{min} of −41.5 dB and 31.1 dB [29,30]; At 2.2 mm, the RL_{min} of wood-texture-column like $NiCo_2O_4$ is −49.73 dB, while the outstanding EAB is 7.10 GHz [31,32]. With the increasing of eddy current loss, interface and dipole polarization due to the morphologies change, the absorption capacity of EMW has been greatly enhanced [33]. This research signed that different morphologies of the same material will effect the ability to absorb EMW.

In the current study, $MnCo_2O_{4.5}$ microsphere clusters, $MnCo_2O_{4.5}$ microcubic spheres and $MnCo_2O_{4.5}$ flowery spheres were prepared by one-step hydrothermal and annealing process. $MnCo_2O_{4.5}$ with different morphologies can be obtained by selecting different organic solutions, different hydrothermal temperatures and time, and their EMW absorption mechanism is explored. $MnCo_2O_{4.5}$ microcubic sphreres exhibited an terrific EAB of 5.36 GHz at 2.3 mm and a RL_{min} of −51.52 dB at 2.2 mm that covering most of the X-band. The change of the morphologies leads to the tunability of the parameters of the composite medium, the improvement of impedance matching and the enhancement of the polarization relaxation process, thus improving the performance in EMW absorption. The absorption of the material changes. In the field of EMW absorption, there are relatively few studies on $MnCo_2O_{4.5}$. Therefore, this work provides a convenient way for the application of morphology-controlled materials in EMW absorption, and provides an idea for efficient X-band microwave absorption of composite materials based on $MnCo_2O_{4.5}$ nanomaterials.

2. Experimental section

2.1. Materials

Manganese (II) acetate tetrahydrate ($Mn(AC)_2{\cdot}4H_2O$),cobalt (II) acetate tetrahydrate ($Co(AC)_2{\cdot}4H_2O$), cobalt nitrate ($Co(NO_3)_2$), urea (CH_4N_2O) and polyvinylpyrrolidone (PVP-K30) were obtained from Sinopharm Reagent Co., Ltd. Ethylene glycol($(CH_2OH)_2$), ethyl alcohol (C_2H_5OH), glycerol ($C_3H_8O_3$) were purchased from Shanghai Macklin Biochemical Co., Ltd. All reagents were analytically pure and could be used directly without further purification.

2.2. Preparation of $MnCo_2O_{4.5}$ microsphere clusters

Firstly, 1 mmol of $Mn(Ac)_2{\cdot}4H_2O$, 2 mmol of $Co(NO_3)_2$ and 20 mmol of urea were dissolved in 30 mL of anhydrous ethanol by ultrasonic processing. Next, the mixed solution was transferred to an autoclave for reaction at 160 °C for 18 h. The precursor was obtained by centrifugation. Finally, after drying at 60 °C for 10 h, the precursor was calcined in the air at 350 °C for 4 h to get the final sample. The $MnCo_2O_{4.5}$ microsphere clusters we prepared were marked as MCO-MCs.

2.3. Preparation of $MnCo_2O_{4.5}$ microcubic spheres

In the beginning, 1 mmol of $Mn(Ac)_2{\cdot}4H_2O$, and 2 mmol of $Co(Ac)_2{\cdot}H_2O$ and appropriate amount of PVP-K30 were dissolved in 80 mL glycol. Then, the mixed solution was transferred to an autoclave for reaction at 220 °C for 24 h. The precursor was made by centrifugation. Eventually, after drying at 60 °C for 10 h, the precursor was calcined in the air at 500 °C for 4 h to get the oxide. The $MnCo_2O_{4.5}$ microsphere clusters we prepared were marked as MCO-MSs.

2.4. Preparation of $MnCo_2O_{4.5}$ flowery spheres

First of all, 1 mmol of $Mn(Ac)_2{\cdot}4H_2O$, 2 mmol of $Co(Ac)_2{\cdot}H_2O$ and appropriate amount of PVP-K30 were put in 80 mL glycol by being stirred for 2 h. Secondly, the mixture was shifted to an autoclave for reaction at 220 °C for 24 h. The precursor was made by centrifugation. In the end, after drying at 60 °C for 10 h, the precursor was calcined in the air at 500 °C for 4 h. The $MnCo_2O_{4.5}$ microsphere clusters we prepared were marked as MCO-FSs.

2.5. Characterization

The X-ray diffraction pattern of the samples was analyzed by powder X-ray diffractometer with Cu-Ka as radiation source (λ =0.15418 nm). The morphologies and elemental mapping of the samples were observed with a field emission scanning electron microscope (SEM, JEOL JSM-7800F), and the lattice spacing of the samples was observed with a transmission electron microscope (TEM, JEOL JEM-2100). The chemical composition was recorded by X-ray photoelectron spectroscopy (XPS, Thermo Escalab 250XI) and Fourier transform infrared spectroscopy (FT-IR, Nicolet iS50).

2.6. Electromagnetic parameters

The prepared sample powder was uniformly mixed with paraffin wax (the mass ratio of sample powder to paraffin wax was 1:1). Through a cylindrical mold with outer diameter of 7 mm and inner diameter of 3.04 mm, the mixed sample was pressed into a ring-shaped sample with a thickness of about 2 mm. The electromagnetic parameters complex permittivity $\varepsilon_r(\varepsilon_r=\varepsilon'-j\varepsilon'')$ and complex permeability $\mu_r(\mu_r=\mu'-j\mu'')$ were measured by coaxial method on a vector network analyzer (VNA, AgilentN5222A) [34]. The frequency range is 2–18 GHz. The RL_{min} value can be calculated according to the transmission line theory, through the following formula [35]:

$$Z_{in} = Z_0\sqrt{\frac{\mu_r}{\varepsilon_r}}\tanh\left(j\frac{2\pi fd}{c}\sqrt{\varepsilon_r\mu_r}\right) \quad (1)$$

$$RL(db) = 20\log\frac{Z_{in}-Z_0}{Z_{in}+Z_0} \quad (2)$$

where Z_{in} and Z_0 represent the input impedance of the standard absorbing material and the characteristic impedance of free space, respectively, f represents the frequency of the EMW, d represents the thickness of the sample, and c represents the speed of the EMW in free space [36].

3. Results and discussion

Experimental procedures of $MnCo_2O_{4.5}$ spinel crystal structure with different morphologies is shown in Fig. 1. $MnCo_2O_{4.5}$ can be successfully prepared by hydrothermal reaction of manganese and cobalt salts as precursors and subsequent calcination process. Notably, the modulation

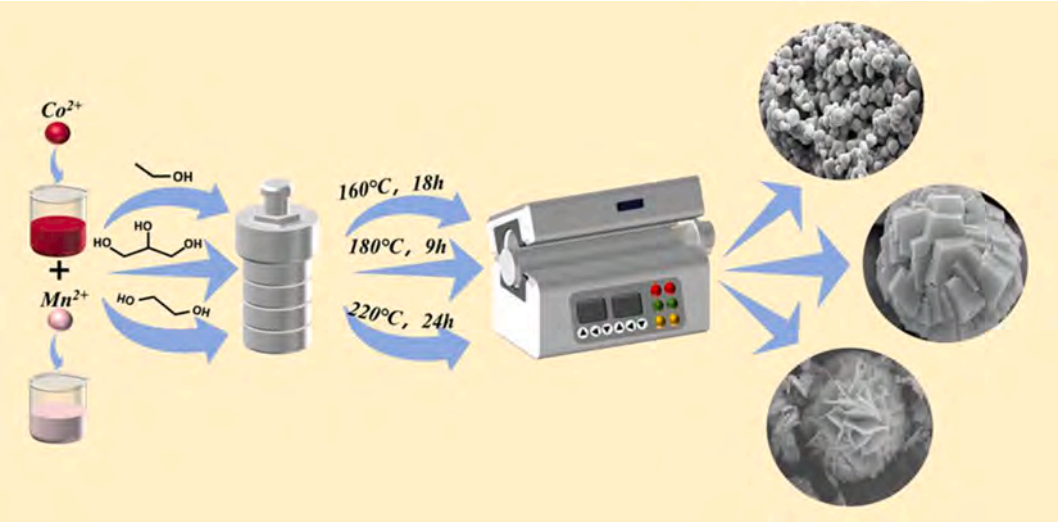

Fig. 1. Schematic diagram of the preparation of three samples.

of the nanostructure of the $MnCo_2O_{4.5}$ spinel material can be achieved by simply modifying the type of solvent and changing the hydrothermal reaction conditions to produce three different morphologies of microsphere clusters, microcubic spheres, and flower-like spheres.

The crystal structures of the three morphologies of $MnCo_2O_{4.5}$ were analyzed by XRD. In Fig. 2a, the peaks at 2θ =19.00°, 31.26°, 36.82°, 38.51°, 44.83°, 55.77°, 59.47°, 65.34°in correspondence with (111), (220), (311), (222), (400), (422), (511), and (440) crystal planes of $MnCo_2O_{4.5}$ (PDF#32–0297). In addition, we compared the prepared XRD patterns of MCO-MSs with the data of $MnCo_2O_4$ (PDF#32–1237) and it can be seen that there are obvious differences. No other characteristic peaks such as $MnCo_2O_4$ or many types of other manganese oxides were found in the XRD curves, demonstrating unadulterated $MnCo_2O_{4.5}$ samples were obtained after calcination in air [37–39]. The FT-IR spectra in Fig. 2b showed the peaks at 552 cm^{-1} and 654 cm^{-1} belong to the Co-C stretching modes derived from interaction of metal bonds [40]. In addition, the peaks near 1618 cm^{-1}, 2980 cm^{-1} and 3409 cm^{-1} were caused by the C–H, C=O and H-O vibration [41]. The data of FT-IR spectrum indicated the preparation of morphology-controlled $MnCo_2O_{4.5}$.

The element valence state of MCO-MSs was estimated by X-ray photoelectron spectroscopy characterization. The full spectrum (Fig. 2c) shows that there are Mn, Co and O elements in MCO-MSs. In Fig. 2b, the characteristic peaks of Co $2p_{1/2}$ and Co $2p_{3/2}$ are 794.61 and 779.23 eV, the peaks of 783.65 and 796.71 eV belong to Co^{2+}, and the peaks of 780.30 and 794.91 eV belong to Co^{3+}. In addition, the peaks of Mn $2p_{3/2}$ and Mn $2p_{1/2}$ correspond to 642.41 and 652.17 eV [42,43]. It could obtain that the peak at 641.22 eV is attributed to Mn^{2+}, and the peaks at 641.22 and 653.70 eV due to Mn^{3+} by analyzing the data (Fig. 2e). From Fig. 2f, the O 1 s spectrum shows peaks at 528.7 eV, 530.9 eV, and 531.5 eV, which included the different oxygens in the A-O (*A*=Mn, Co) metal bond, in hydroxyl groups, and in H_2O absorbed by MCO-MSs, respectively.[44] Above all, the XPS data bore out that Co^{2+}, Co^{3+}, Mn^{2+}, and Mn^{3+} appeared at the same time in MCO-MSs, and it substantiated the successful preparation of $MnCo_2O_{4.5}$ mirocubic spheres one-step hydrothermal and annealing process.

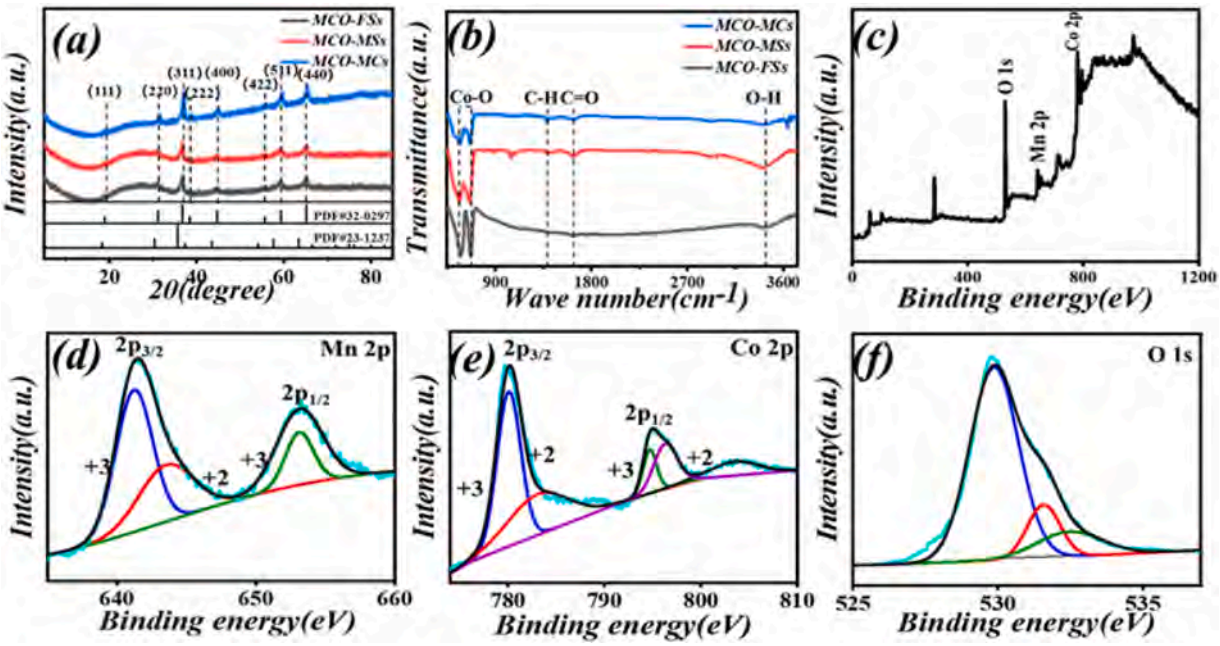

Fig. 2. (a) XRD patterns and (b) FT-IR pattern of all samples; XPS spectra of (c) survey spectrum for all samples, (d) O 1 s, (e) Mn 2p, (f) Co 2p for MCO-MSs.

In order to compare the morphological differences of $MnCo_2O_{4.5}$ with different structures, scanning electron microscope imaging was carried out. From Fig. 3a–c, it is found that, MCO-MSs are formed by a large number of small cubes, MCO-MCs has a solid spherical structure with cluster aggregation, MCO-FSs has a flower structure. As can be seen from Fig. 2b1 and c1, the dimensions of MCO-MSs and MCO-FSs are about 1 μm. The size of MCO-MCs is much smaller than the other two samples. The above results show that different solvents, hydrothermal time and temperature have profound effects on the microstructure of samples, in which the change of morphologies has a crucial effect, leading to the difference in the capacity of EMW absorption. The Fig. 3d–f shows the corresponding element distribution of Co, Mn and O in the MCO-MSs. As shown in Fig. 3d–f, the morphology of MCO-MSs was analyzed by TEM and HRTEM characterization [45]. From Fig.3d, it showed that MCO-MSs has a solid construction, distinctly different from the cobalt spinel structure oxides with hollow structure like $ZnCo_2O_4$ which was prepared before. The ED ring is composed of dispersive points [46]. The TEM image showed shows various lattice fringes in diverse directions. The TEM image of MCO-MSs in the figure shows a face spacing of 0.235 nm and 0.164 nm due to the (222) and (422) crystal faces of MCO-MSs [47]. The diffraction rings of the MCO-MSs (222), (422), and (511) crystal faces can be clearly seen in Fig. 3f. The results of HRTEM and SAED analysis further prove the successful preparation of $MnCo_2O_{4.5}$.

The capacities in EMW absorbing of paraffin coatings when the micromatials were used as fillers were investigated by using paraffin as the substrate and preparing each sample powder as a circular sample [48]. Firstly, the complex permittivity ($\varepsilon_r = \varepsilon' - j\varepsilon''$) and complex permeability ($\mu_r = \mu' - j\mu''$) of the materials were recorded by a vector network analyzer, which is significant for making sure the EMW absorption properties of the absorbers [49]. To our knowledge, the real (ε') and imaginary (ε'') parts of the complex permittivity constants point to the storage and loss capacities of electrical energy, and the real (μ') and imaginary (μ'') parts of the complex permeability are represented as the storage and dissipation capacities of magnetic energy [50].

The complex permittivity parameter and dielectric loss factor ($tan\delta_\varepsilon$) of MCO with multiple morphology are shown in Fig. 4a–c, and it can be observed that there is a significant difference in the dielectric performance of MCO spinel materials with different structures [51]. It is worth noting that there is a significant fluctuation in the 9–14 GHz range for

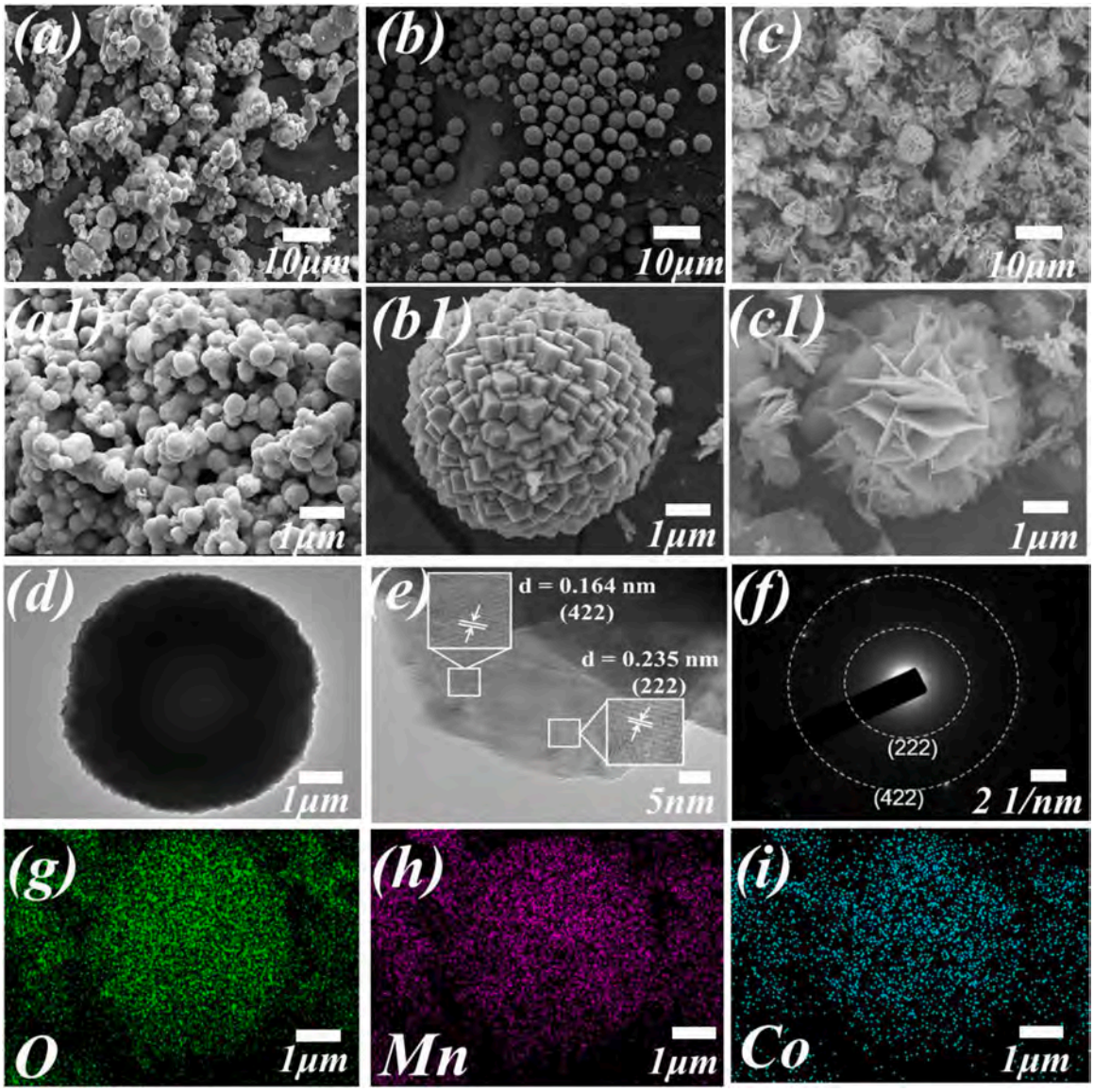

Fig. 3. The SEM images of (a-a1) MCO-MCs, (b-b1) MCO-MSs, (c-c1) MCO-FSs, (e–i) the element mapping images of MCO-MSs. The (d) TEM images, (e) selected electron diffraction images and (f) the element mapping images of MCO-MSs.

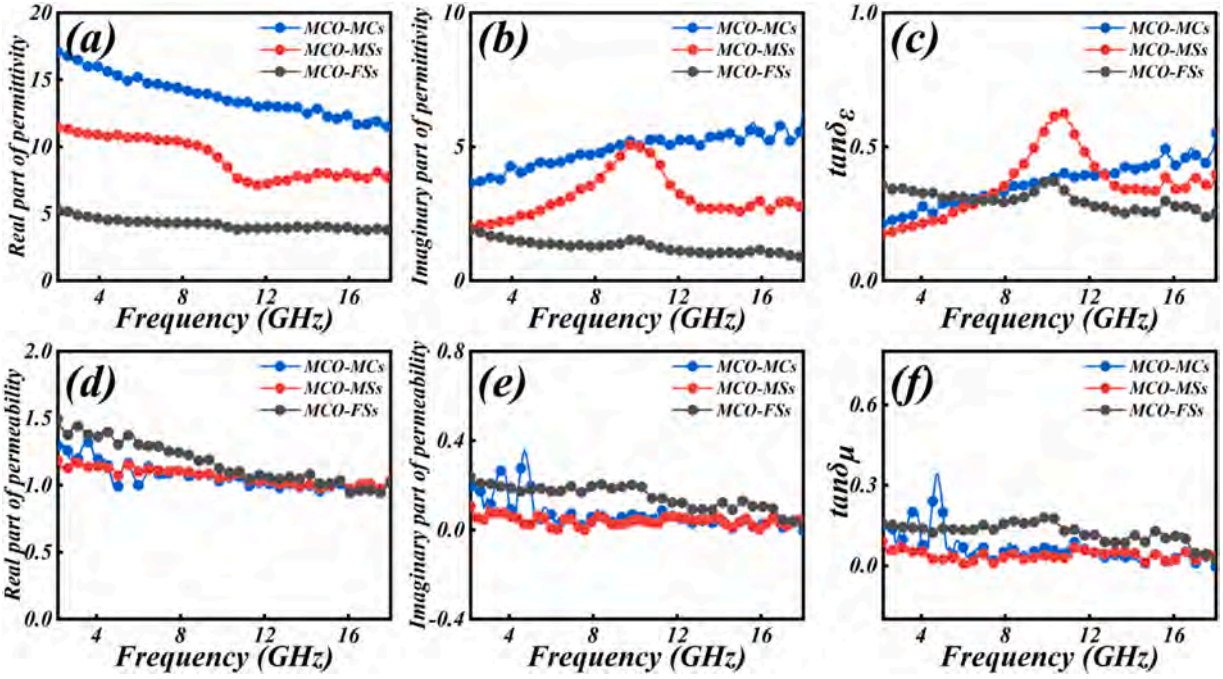

Fig. 4. Electromagnetic parameters. (a) Real part, (b) imaginary part, (c) tangent of permittivity, (d) Real part, (e) imaginary part, (f) tangent of permeability of each sample.

MCO-MSs compared to MCO-MCs and MCO-FSs, which may be caused by their polarization relaxation process in this region. The complex permeability parameter and the magnetic loss factor ($tan\delta_\mu$) of all samples are shown in Fig. 4d–. It indicates clearly the complex permeability parameter of each sample is low compared to the level and dielectric properties of the tanδ_μ curve [52].

From the average values of tanδ_ε and tanδ_μ (Fig. 5a), it presents evidently that the dielectric loss capability of the various samples far exceeds the magnetic loss level, which suggests that the dielectric loss dominates in this work as the main EMW loss mechanism [53]. In general, the C_0 curve is available for investigating the magnetic loss mechanism of the absorbers. The expression is as below [54]:

$$C_0 = \mu''(\mu')^{-2}f^{-1} \tag{3}$$

As can be seen in Fig. 5b, each spinel sample, especially the MCO-MCs, has volatility in 4–8 GHz, which indicates the existence of natural resonance [55]. Furthermore, the C_0 of each sample shows almost no fluctuation in 8–18 GHz, it signifies eddy current losses dominate during this region [56].

The attenuation constant (α) is a combination of the dielectric/

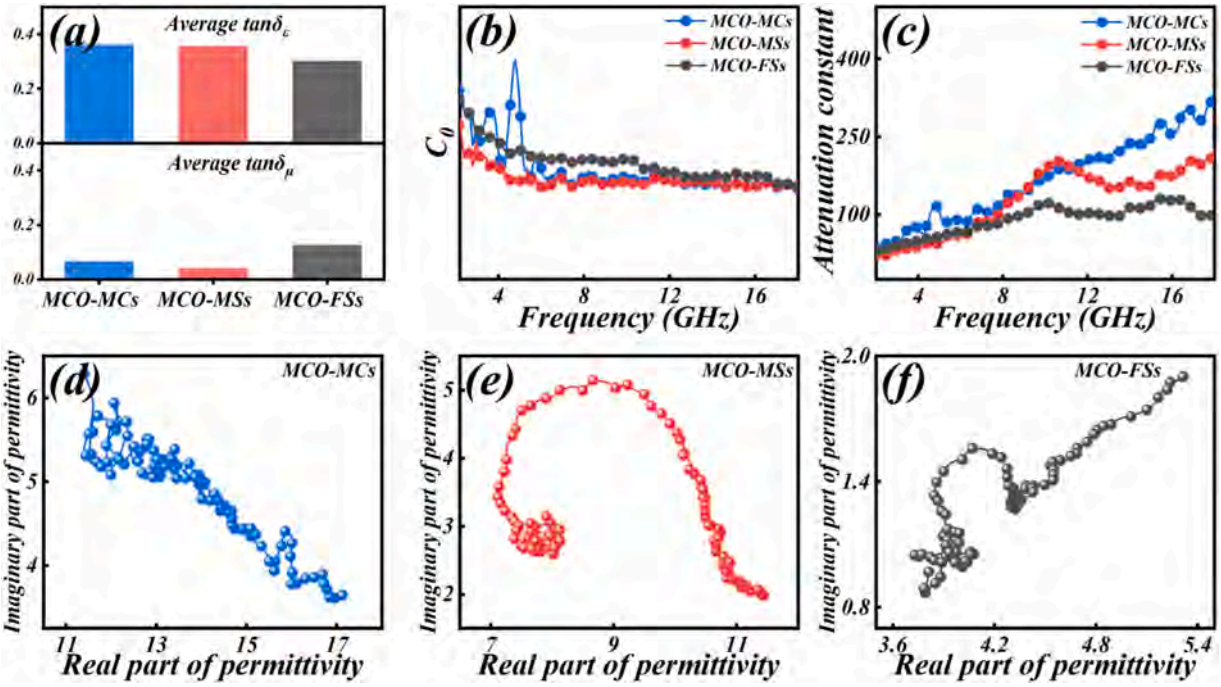

Fig. 5. Average tangent (a) of the permittivity and permeability, C_0 (b), attenuation constant (c) and Cole-Cole diagram (d–f) of each sample.

magnetic performance of a material's ability to attenuate EMW, and is an important factor to keep in mind when designing materials which have fantastic abilities in EMW absorption. The equation is derived as follows [57,58]:

$$\alpha = \frac{\sqrt{2}\pi f}{c}\sqrt{(\mu''\varepsilon'' - \mu'\varepsilon') + \sqrt{(\mu''\varepsilon'' - \mu'\varepsilon')^2 + (\mu'\varepsilon'' + \mu''\varepsilon')^2}} \quad (4)$$

On the whole, among the three samples with different morphologies of MCO spinel structures, the highest level of EMW attenuation is observed for MCO-MCs, followed by MCO-MSs and MCO-FSs [59,60]. The α (Fig. 5c) and tanδ_ε (Figs. 4c and 5b) of each sample show a similar trend, which further demonstrates that the dielectric loss prevails in theory. More significantly, it proves the rationality of the modulation of dielectric properties and loss mechanisms through structural design [61, 62].

For revealing the dielectric loss mechanism, we adopt the Debye principle to illustrate the polarization relaxation behavior with the following equations [63,64]:

$$\varepsilon' = \frac{1}{2\pi\tau}\frac{\varepsilon''}{f} + \varepsilon_\infty \quad (5)$$

$$\varepsilon'' = \frac{\omega\tau(\varepsilon_s - \varepsilon_\infty)}{1 + (2\pi f)^2 r^2} \quad (6)$$

The ε_∞ and ε_s, τ and f are symbols of the optical permittivity and static permittivity, polarization relaxation time and frequency [65,66]. The Cole-Cole equation can be formulated as below [67,68]:

$$\left(\varepsilon' - \frac{\varepsilon_s + \varepsilon_\infty}{2}\right)^2 + (\varepsilon'')^2 = \left(\frac{\varepsilon_s - \varepsilon_\infty}{2}\right)^2 \quad (7)$$

According to Eq. (7), if a polarization relaxation process survives in the material, the graphs plotted by ε'' and ε' would appear as semicircular arcs, with each arc is a symbol of a Debye relaxation process [69, 70]. Compared with MCO-MCs, Cole-Cole images of MCO-MSs and MCO-FSs show an obvious semicircular shape (Fig. 5d–f), indicating that there is an obvious polarization relaxation process between the two. This can be explained by the strong interfacial polarization between the material and the free space due to its unique topography. The above results strongly reveal that the introduction of polarization relaxation process through structural engineering strategy, which in turn subserves the raise of the dielectric properties of the materials [71,72].

According to the previous researches, the preparation of the EMW absorber need to think of the impedance matching performance of the nanomaterials in addition to the requirement of attenuation ability [73]. The impedance matching performance indicates the accessibility of the EMW to the inside of the nanomaterials and is an essential bussiness for the attenuation ability to work. The formula for deriving the measured value Z is as follows [74]:

$$Z = \frac{Z_{in}}{Z_0} = \sqrt{\frac{\mu_r}{\varepsilon_r}}\tanh\left(j\frac{2\pi fd}{c}\sqrt{\varepsilon_r\mu_r}\right) \quad (8)$$

The Z value is related to the thickness (d) and frequency (f), and as the Z value approaches 1, the EMW inclines to travel inside the material without reflection, signifing that an impedance match has been attained [75]. Fig. 6 shows the impedance matching plot for MCO-MCs, MCO-MSs, and MCO-FSs. The yellow area between $Z = 0.8$ and $Z = 1.2$ is circled in black, with the circled area representing a higher degree of impedance match. Notably, the MCO-MCs with the strongest dielectric performance have the poorest impedance matching performance. According to previous research, the ability of EMW to enter a material is related to the material's impedance matching, which is related to the material's structure and dielectric parameters. High dielectric parameters can lead to impedance mismatch, resulting in more EMW being reflected than entering the material. Therefore, MCO-FSs exhibits better impedance matching performance than MCO-FCs, which makes it have better EMW absorption performance. The impedance matching performance of all samples showed an opposite trend to the permittivity parameter, which can be put down to the impedance mismatch phenomenon caused when the permittivity parameter is too high. Based on the above conclusions, the combination of excellent EMW attenuation ability and splendid impedance matching will give the MCO-MSs the awesome capacity in EMW absorption.

In light with the line transmission theories, RL and EAB are counted in the light of Eqs. (1) and (2), so that capacities in EMW absorption of the material can be assessed more intuitively. On account of the calculation results, the absorption of incident EMW will achieve 90 % when RL<−10 dB. As a result, in the 2D and 3D RL diagrams (Fig. 7), the area with RL<−10 dB is marked with a black line, which is the region of EAB. Combining the fantastic attenuation capability and good impedance matching of MCO-MSs, it revealed the lowest RL_{min} in theory and the excellent EAB_{max} (−51.52 dB for RL_{min} at 2.2 mm, and 5.36 GHz for EAB_{max} at 2.3 mm) at a thin thickness [76]. In addition, in order to gain more insight into the EMW absrption behavior of MCO spinel materials, we use the quarter-wavelength matching theory to explore the relationship between the matching thickness and the RL_{min} and frequency. The formula is as described below [77]:

$$t_m = \frac{n\lambda}{4} = \frac{nc}{4f_m\sqrt{|\mu_r||\varepsilon_r|}}(=1,3,5.....) \quad (9)$$

Where t_m is the matching thickness, c is the velocity of the EMW in vacuum, f_m is the matching frequency, and $|\varepsilon_r|$ and $|\mu_r|$ are the moduli of ε_r and μ_r [78].

If the phase difference between the reflected and absorbed waves reaches 180°, then t_m and f_m satisfy the above equation and the two waves cancel each other out. More importantly, the RL_{min} of the nanomaterials is going to achieve the minimum value, i.e., RL_{min} [79]. According to Fig. 8, with the increase of the thickness, the RL_{min} is gradually transformed to the low frequency. The experimental consequence are consistent with the simulation leads to t_m-f_m curves and also confirm that the quarter-wavelength matching model could accurately describe the abilities in EMW absorption.

Dielectric loss and magnetic loss are the main ways for absorber to

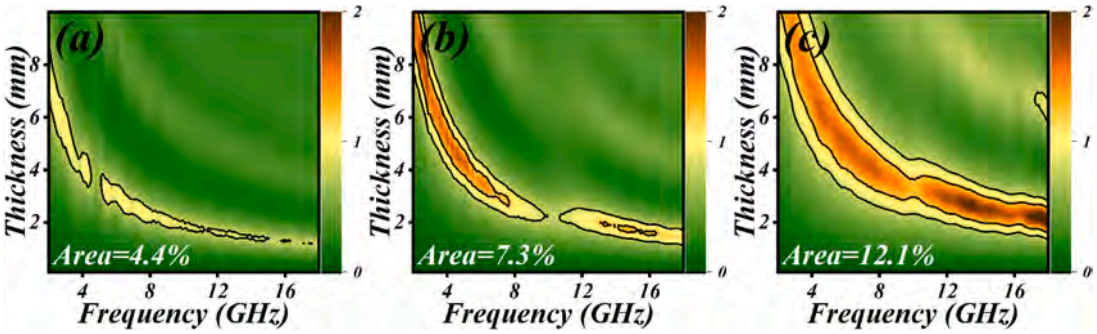

Fig. 6. The normalized input impendence Z of (a) MCO-MCs, (b) MCO-MSs and (c) MCO-FSs.

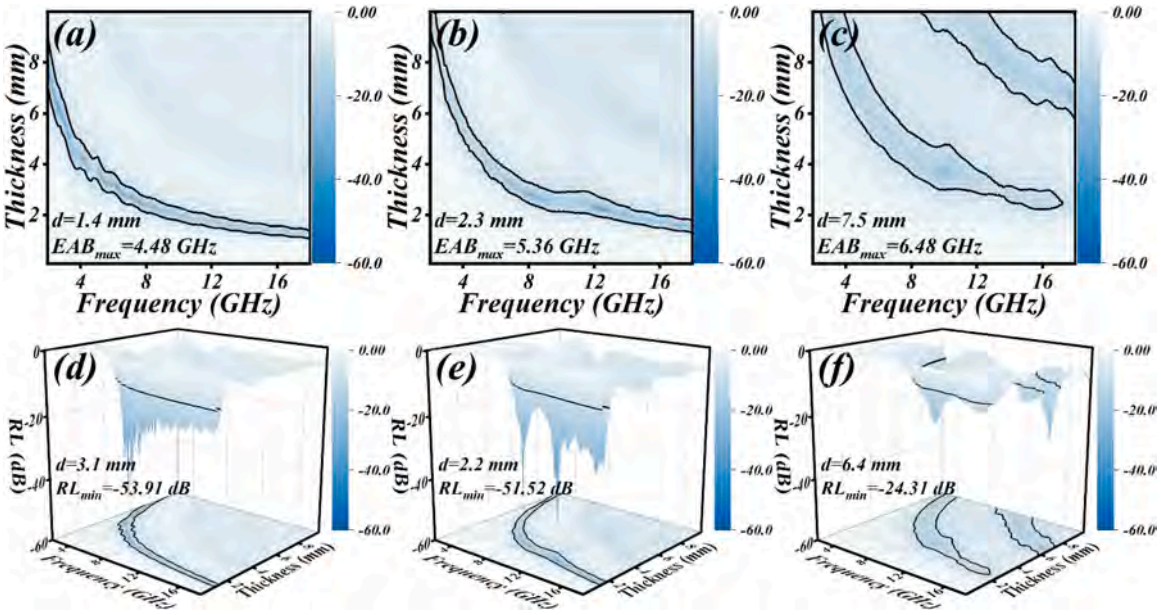

Fig. 7. The 2D (a-c) and 3D (d-f) RL of MCO-MCs, MCO-MSs and MCO-FSs.

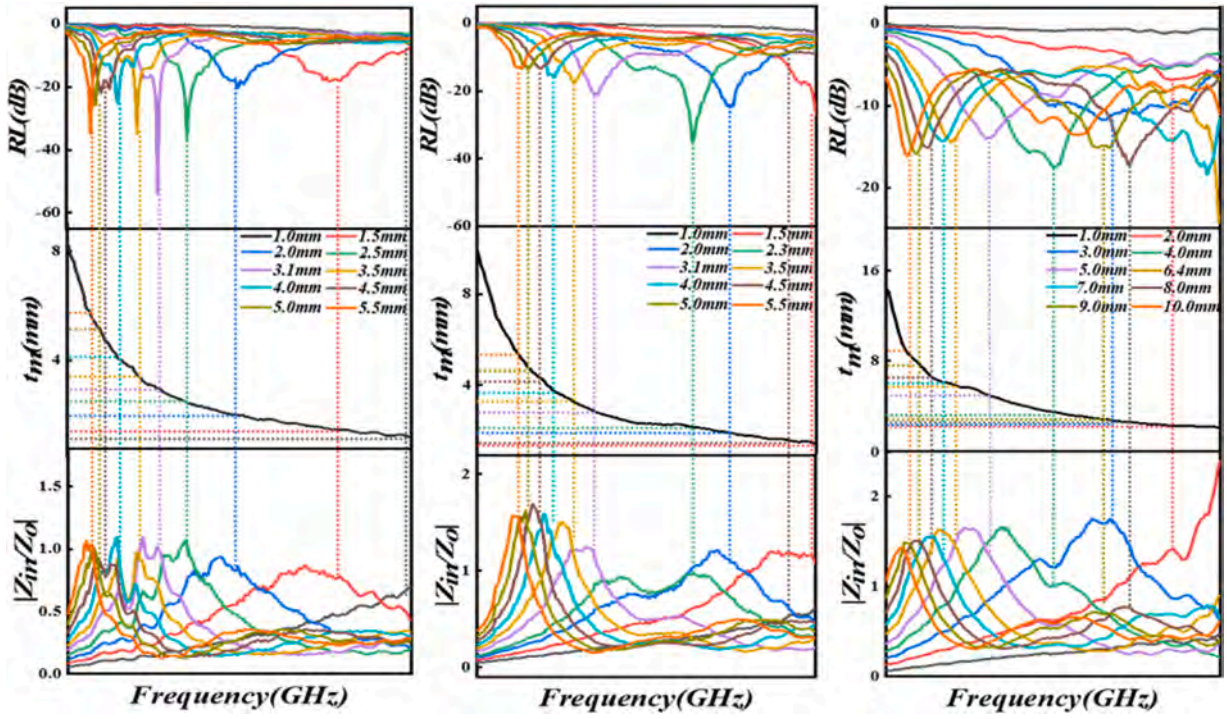

Fig. 8. Correlation diagram of (a) MCO-MCs, (b) MCO-MSs, (c) MCO-FSs RL_{min} value and $|Z_{in}/Z_0|$ under λ/4 matching thickness.

attenuate EMW. Dielectric loss is usually determined by conduction loss, interface polarization, and multiple scattering. Polarization relaxation is mainly caused by dipole and interface polarization. Dipoles are generated at the positions of functional groups, defects, and interfaces. Under high frequency alternating electric field, when the dipole rotation can not follow the change of the electric field, the dipole directional polarization loss will occur, which is the key role of dielectric loss [80,81]. The fantastic capacities in EMW absorption of the MCO-MSs due to the syneries of impedance matching and dielectric/magnetic loss theories (Fig. 9). Based on the former analyzing information of the permeability parameters, the magnetic properties of MCO include magnetic resonance and eddy current losses. The dielectric loss prevailed the attenuation properties of MCO. In addition, the unique morphology of the microcubic spheres of MCO induces stronger interfacial polarization. In conclusion, the EMW absorption performance of MCO-MSs was fully optimized under the combined effect of multiple mechanisms. Table 1 presents typical AB_2O_4 absorbers and their optimal EMW absorption properties. It can be clearly seen that $MnCo_2O_{4.5}$ are significantly competitive compared to th Co-based electromagnetic absorbers.

4. Conclusion

Ultimately, a series of morphology-controlled MCO spinel oxides were prepared by hydrothermal and thermal treatments in this study.

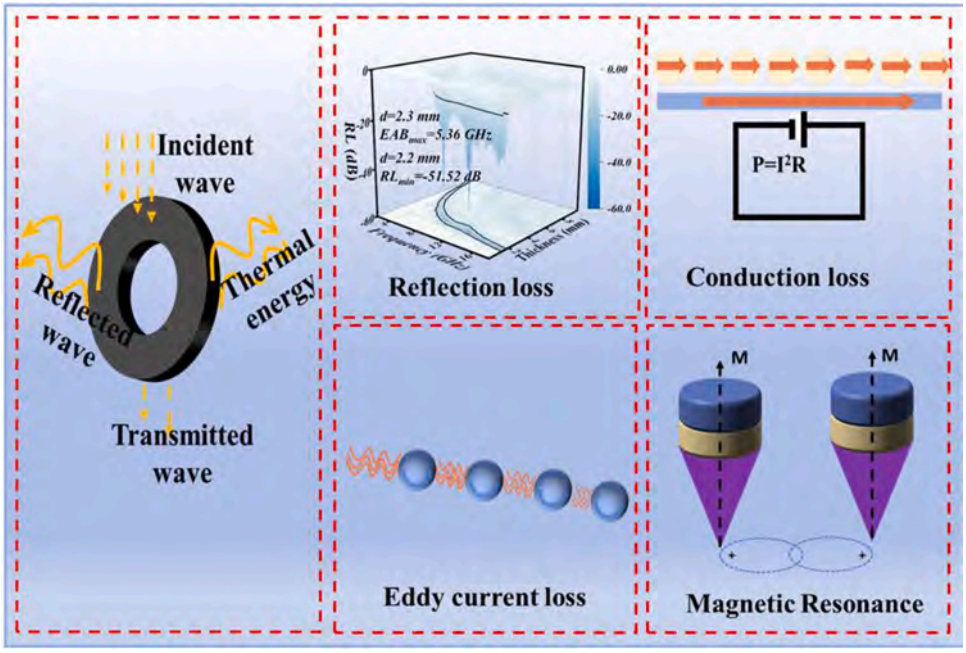

Fig. 9. EMW absorption mechanism of MCO-MSs.

Table 1
Comparison of EMW absorption performance with other materials.

Absorber	Content (wt%)	RL_{min} (dB)	Thickness (mm)	EAB (GHz)	Refs.
$MnCo_2O_4$	60	−43	2.5	4.4	[17]
$MnCo_2O_{4.5}$@Co_2NiO_4	70	−40.01	2.00	6.12	[18]
$MnFe_2O_4$	30	−40.4	3.0	6.8	[56]
$ZnCo_2O_4$	70	−52.9	3.5	4. 48	[21]
$NiCo_2O_4$	45	−39	2.5	3	[23]
$NiCo_2O_4$	45	−45	4	3.5	[23]
$NiCo_2O_4$	45	−40.0	1.4	6.0	[23]
Co_2SiO_4	25	−46.7	2.9	5.92	[35]
$CuFe_2O_4$	30	−48.81	4.0	4.08	[11]
S1	50	−53.91	3.1	4.48	This work
S2	50	−51.48	2.3	5.36	This work
S3	50	−24.31	6.4	6.48	This work

Based on the importance of the structural design of EMW absoption materials, three different morphologies of MCO, namely, microspheres, microcubes and flower spheres, were successfully prepared by modulating the experimental conditions. Remarkably, the MCO-MSs achieved outstanding capabilities in EMW absorption with a RL_{min} of −51.52 dB at 2.2 mm and an EAB_{max} of 5.36 GHz at 2.3 mm. This strategy was used to modulate the complex dielectric parameters of the materials through the improvement of the morphologies and to adjust the impedance matching, more importantly, to enhance the polarization relaxation process. This work supplies guidance for adjusting the EMW absorption abilities of cobalt-based spinel oxides designed highly outstanding EMW absorbing coatings in the X-band.

CRediT authorship contribution statement

Yun Han: Writing – original draft. **Mengjun Han:** Writing – original draft. **Tianbao Zhao:** Writing – original draft. **Zihao Xia:** Data curation. **Jiaxiao Zou:** Formal analysis. **Xuehua Liu:** Writing – review & editing. **Zirui Jia:** Writing – review & editing.

Declaration of Competing Interest

The authors declare that they have no known competing financial interests or personal relationships that could have appeared to influence the work reported in this paper.

Data availability

No data was used for the research described in the article.

Acknowledgments

This work is financially supported by the National Natural Science Foundation of China (No.52377026 and No. 52301192), Natural Science Foundation of Shandong Province (No.ZR2019YQ24), Taishan Scholars and Young Experts Program of Shandong Province (No. tsqn202103057), the Qingchuang Talents Induction Program of Shandong Higher Education Institution (Research and Innovation Team of Structural-Functional Polymer Composites) and Special Financial of Shandong Province (Structural Design of High-efficiency Electromagnetic Wave-absorbing Composite Materials and Construction of Shandong Provincial Talent Teams).

References

[1] Y. Wang, X. Gao, L.J. Zhang, X.M. Wu, Q.G. Wang, C.Y. Luo, G.L. Wu, Synthesis of Ti_3C_2/Fe_3O_4/PANI hierarchical architecture composite as an efficient wide-band electromagnetic absorber, Appl. Surf. Sci. 480 (2019) 830–838.
[2] G.L. Wu, Y.H. Cheng, Z.H. Yang, Z.R. Jia, H.J. Wu, L.J. Yang, H.L. Li, P.Z. Guo, H. L. Lv, Design of carbon sphere/magnetic quantum dots with tunable phase compositions and boost dielectric loss behavior, Chem. Eng. J. 333 (2018) 519–528.
[3] M. Cao, Y. Cai, P. He, J. Shu, W. Cao, J. Yuan, 2D MXenes: electromagnetic property for microwave absorption and electromagnetic interference shielding, Chem. Eng. J. 359 (2018) 1265–1302.
[4] S.J. Zhang, B. Cheng, Z.G. Gao, D. Lan, Z.W. Zhao, F.C. Wei, Q.S. Zhu, X.P. Lu, G. L. Wu, Two-dimensional nanomaterials for high-efficiency electromagnetic wave absorption: an overview of recent advances and prospects, J. Alloy. Compd. 893 (2022) 16234.
[5] H.L. Lv, X.D. Zhou, G.L. Wu, U.I. Kara, X.G. Wang, Engineering defects in 2D g-C_3N_4 for wideband, efficient electromagnetic absorption at elevated temperature, J. Mater. Chem. A 9 (2021) 19710–19718.

[6] X. Shu, S. Yan, B. Fang, Y. Song, Z. Zhao, A 3D multifunctional nitrogen-doped RGO-based aerogel with silver nanowires assisted self-supporting networks for enhanced electromagnetic wave absorption, Chem. Eng. J. 451 (2022) 138825.
[7] X.F. Zhou, Z.R. Jia, A.L. Feng, X.X. Wang, J.J. Liu, M. Zhang, H.J. Cao, G.L. Wu, Synthesis of fish skin-derived 3D carbon foams with broadened bandwidth and excellent electromagnetic wave absorption performance, Carbon 152 (2019) 827–836.
[8] X. Sun, Y. Li, Y. Huang, Y. Chen, S. Wang, W. Yin, Achieving super broadband electromagnetic absorption by optimizing impedance match of rGO sponge metamaterials, Adv. Funct. Mater. 32 (2021) 2107508.
[9] Y. Guo, K. Ruan, G. Wang, J. Gu, Advances and mechanisms in polymer composites toward thermal conduction and electromagnetic wave absorption, Sci. Bull. 68 (2023) 1195–1212.
[10] X.Y. Zhang, Z.R. Jia, F. Zhang, Z.H. Xia, J.X. Zou, Z. Gu, G.L. Wu, MOF-derived $NiFe_2S_4$/Porous carbon composites as electromagnetic wave absorber, J. Colloid Interface Sci. 610 (2022) 610–620.
[11] S. Deng, H. Ai, B. Wang, Research on the electromagnetic wave absorption properties of GNPs/EMD cement composite, Constr. Build. Mater. 321 (2022) 126398.
[12] H. Zhang, K. Sun, K. Sun, L. Chen, G. Wu, Core-shell Ni_3Sn_2@C particles anchored on 3D N-doped porous carbon skeleton for modulated electromagnetic wave absorption, J. Mater. Sci. Technol. 158 (2023) 242–252.
[13] B. Sun, S. Sun, P. He, H. Mi, B. Dong, C. Liu, C. Shen, Asymmetric layered structural design with segregated conductive network for absorption-dominated high-performance electromagnetic interference shielding, Chem. Eng. J. 416 (2021) 129083.
[14] X. Yan, X. Huang, B. Zhong, T. Wu, H. Wang, T. Zhang, N. Bai, G. Zhou, H. Pan, G. Wen, L. Xia, Balancing interface polarization strategy for enhancing electromagnetic wave absorption of carbon materials, Chem. Eng. J. 391 (2019) 123538.
[15] J.W. Wang, B.B. Wang, Z. Wang, L. Chen, C.H. Gao, B.H. Xu, Z.R. Jia, G.L. Wu, Synthesis of 3D flower-like ZnO/$ZnCo_2O_4$ composites with the heterogeneous interface for excellent electromagnetic wave absorption properties, J. Colloid Interface Sci. 586 (2021) 479–490.
[16] L. Li, G. Li, W. Ouyang, Y. Zhang, F. Zeng, C. Liu, Z. Lin, Bimetallic mofs derived FeM(II)-alloy@C composites with high-performance electromagnetic wave absorption, Chem. Eng. J. 420 (2020) 127609.
[17] S. Masoudpanah, Microwave absorption properties of $ZnCo_2O_4$ and $MnCo_2O_4$ powders synthesized by oxalate-assisted hydrothermal method, J. Mater. Res. Technol. 20 (2022) 3750–3759.
[18] Y. Zhang, S. Tan, Z. Zhou, X. Guan, Y. Liao, C. Li, G. Ji, Construction of Co_2NiO_4@$MnCo_2O_{4.5}$ nanoparticles with multiple hetero-interfaces for enhanced electromagnetic wave absorption, Particuology 81 (2023) 81–97.
[19] S. Dong, X. Zhang, P. Hu, W. Zhang, J. Han, P. Hu, Biomass-derived carbon and polypyrrole addition on SiC whiskers for enhancement of electromagnetic wave absorption, Chem. Eng. J. 359 (2018) 882–893.
[20] Z. Chen, K. Tian, C. Zhang, R. Shu, J. Zhu, Y. Liu, Y. Huang, X. Liu, *In-situ* hydrothermal synthesis of NiCo alloy particles@hydrophilic carbon cloth to construct corncob-like heterostructure for high-performance electromagnetic wave absorbers, J. Colloid Interface Sci. 616 (2022) 823–833.
[21] J. Wang, B. Wang, A. Feng, Z. Jia, G. Wu, Design of morphology-controlled and excellent electromagnetic wave absorption performance of sheet-shaped $ZnCo_2O_4$ with a special arrangement, J. Alloy. Compd. 834 (2020) 155092.
[22] G. Wang, C. Li, D. Estevez, P. Xu, M. Peng, H. Wei, F. Jin, Boosting interfacial polarization through heterointerface engineering in MXene/graphene intercalated-based microspheres for electromagnetic wave absorption, Nano Micro Lett. 15 (2023) 152.
[23] Y. Zhang, S. Gao, J. He, F. Wei, X. Zhang, CoFe@C composites decorated with residual carbon as an ultrathin microwave absorber in the X and Ku bands, Diam. Relat. Mater. 41 (2024) 110666.
[24] T.Q. Hou, B.B. Wang, M.L. Ma, A.L. Feng, Z.Y. Huang, Y. Zhang, Z.R. Jia, G.X. Tan, H.J. Cao, G.L. Wu, Preparation of two-dimensional titanium carbide ($Ti_3C_2T_x$) and $NiCo_2O_4$ composites to achieve excellent microwave absorption properties, Compos. Part B Eng. 180 (2020) 107577.
[25] Z. Zhang, J. Tan, W. Gu, H. Zhao, J. Zheng, B. Zhang, G.B. Ji, Cellulose-chitosan framework/polyailine hybrid aerogel toward thermal insulation and microwave absorbing application, Chem. Eng. J. 395 (2020) 125190.
[26] J.W. Wang, Z.R. Jia, X.H. Liu, J.L. Dou, B.H. Xu, B.B. Wang, G.L. Wu, Construction of 1D heterostructure NiCo@C/ZnO nanorod with enhanced microwave absorption, Nano-Micro Lett. 13 (2021) 175.
[27] L. Rao, L. Wang, C. Yang, R. Zhang, J. Zhang, C. Liang, R. Che, Confined diffusion strategy for customizing magnetic coupling spaces to enhance low-frequency electromagnetic wave absorption, Adv. Funct. Mater. 33 (2023) 2213258.
[28] C. Cui, L. Geng, S. Jiang, W. Bai, L. Dai, S. Jiang, J. Hu, E. Ren, R. Guo, Construction of hierarchical carbon fiber aerogel@hollow Co_9S_8 polyhedron for high-performance electromagnetic wave absorption at low-frequency, Chem. Eng. J. 466 (2023) 134112.
[29] X. Lu, X. Li, Y. Wang, W. Hu, W. Zhu, D. Zhu, Y. Qing, Construction of $ZnIn_2S_4$ nanosheets/3D carbon heterostructure with Schottky contact for enhancing electromagnetic wave absorption performance, Chem. Eng. J. 431 (2021) 134078.
[30] S. Gao, Y. Zhang, H. Xing, H. Li, Controlled reduction synthesis of yolk-shell magnetic@void@C for electromagnetic wave absorption, Chem. Eng. J. 387 (2020) 124149.
[31] Y. Huang, A. Xie, F. Ceidi, W. Zhu, H. Li, S. Yin, X. Xu, H. Xiao, Core-shell heterostructured nanofibers consisting of Fe_7S_8 nanoparticles embedded into S-doped carbon nanoshells for superior electromagnetic wave absorption, Chem. Eng. J. 423 (2021) 130307.
[32] J. Ding, R. Shi, C. Gong, C. Wang, Y. Guo, T. Chen, Y. Zhang, H. Cong, C. Shi, F. He, Defect engineering activates schottky heterointerfaces of graphene/$CoSe_2$ composites with ultrathin and lightweight design strategies to boost electromagnetic wave absorption, Adv. Funct. Mater. (2023) 202305463.
[33] Z.Y. Tong, Z.J. Liao, Y.Y. Liu, M.L. Ma, Y.X. Bi, W.B. Huang, Y. Ma, M.T. Qiao, G. L. Wu, Hierarchical Fe_3O_4/Fe@C@MoS_2 core-shell nanofibers for efficient microwave absorption, Carbon 179 (2021) 646–654.
[34] L. Rao, Z. Liu, L. Wang, W. You, C. Yang, R. Zhang, X. Xiong, L. Yang, H. Zhang, J. Zhang, H. Lv, R. Chao, Dimensional engineering of hierarchical nanopagodas for customizing cross-scale magnetic coupling networks to enhance electromagnetic wave absorption, Adv. Funct. Mater. 33 (2023) 2306984.
[35] Z. Jia, D. Lan, M. Chang, Y. Han, G. Wu, Heterogeneous interfaces and 3D foam structures synergize to build superior electromagnetic wave absorbers, Mater. Today Phys. 37 (2023) 101215.
[36] Y. Xie, Y. Guo, T. Cheng, L. Zhao, T. Wang, A. Meng, M. Zhang, Z. Li, Efficient electromagnetic wave absorption performances dominated by exchanged resonance of lightweight PC/Fe_3O_4@PDA hybrid nanocomposite, Chem. Eng. J. 457 (2022) 141205.
[37] Y. Yao, F. Wu, A. Xie, L. Wu, W. Zhao, X. Zhu, X. Qi, Electrically conductive conjugate microporous polymers (CMPs) via confined polymerization of pyrrole for electromagnetic wave absorption, Chem. Eng. J. 398 (2020) 125591.
[38] G. Wen, X. Zhao, Y. Liu, D. Yan, Z. Hou, Electromagnetic wave absorption performance and electrochemical properties of multifunctional materials: air@$Co@Co_3Sn_2@SnO_2$ hollow sphere/reduced graphene oxide composites, Chem. Eng. J. 420 (2021) 130479.
[39] Y. Qian, Y. Luo, Y. Li, T. Xiong, L. Wang, S. Gang, X. Li, Q. Jiang, J. Yang, Enhanced electromagnetic wave absorption, thermal conductivity and flame retardancy of BCN@LDH/EP for advanced electronic packing materials, Chem. Eng. J. 467 (2023) 143433.
[40] D. Lan, H. Li, M. Wang, Y. Ren, J. Zhang, M. Zhang, L. Ouyang, J. Tang, Y. Wang, Recent advances in construction strategies and multifunctional properties of flexible electromagnetic wave absorbing materials, Mater. Res. Bull. 171 (2023) 112630.
[41] Z. Shen, D. Lan, Y. Cong, Y. Lian, N. Wu, Z. Jia, Tailored heterogeneous interface based on porous hollow In-Co-C nanorods to construct adjustable multi-band microwave absorber, J. Mater. Sci. Technol. 181 (2024) 128–137.
[42] B. Wang, M. Ding, C. Shao, J. Yu, H. Kong, D. Zhao, C. Li, Facile synthesis of Co_xFe_y@C nanocomposite fibers derived from pyrolysis of cobalt/iron chelate nanowires for strong broadband electromagnetic wave absorption, Chem. Eng. J. 465 (2023) 142803.
[43] Y. Yang, L. Xia, T. Zhang, B. Shi, L. Huang, B. Zhong, X. Zhang, H. Wang, J. Zhang, G. Wen, Fe_3O_4@LAS/RGO composites with a multiple transmission-absorption mechanism and enhanced electromagnetic wave absorption performance, Chem. Eng. J. 352 (2018) 510–518.
[44] Z. Xiang, Y. Shi, X. Zhu, L. Cai, W. Lu, Flexible and waterproof 2D/1D/0D construction of MXene-based nanocomposites for electromagnetic wave absorption, EMI shielding, and photothermal conversion, Nano Micro Lett. 13 (2021) 150.
[45] Q. Song, F. Ye, L. Kong, Q. Shen, L. Han, L. Feng, G. Yu, Y. Pan, H. Li, Graphene and mxene nanomaterials: toward high-performance electromagnetic wave absorption in gigahertz band range, Adv. Funct. Mater. 30 (2020) 2000475.
[46] Y. Qian, Y. Tao, Y. Li, J. Hao, C. Xu, W. Yan, Q. Jiang, Y. Luo, J. Jiang, High performance epoxy resin with efficient electromagnetic wave absorption and heat dissipation properties for electron packaging by modification of 3D MDCF@hBN, Chem. Eng. J. 441 (2022) 136033.
[47] X. Lan, Y. Li, Z. Wang, High-temperature electromagnetic wave absorption, mechanical and thermal insulation properties of *in-situ* grown SiC on porous SiC skeleton, Chem. Eng. J. 397 (2020) 125250.
[48] T.Q. Hou, Z.R. Jia, A.L. Feng, Z.H. Zhou, X.H. Liu, H.L. Lv, G.L. Wu, Hierarchical composite of biomass derived magnetic carbon framework and phytic acid doped polyanilne with prominent electromagnetic wave absorption capacity, J. Mater. Sci. Technol. 68 (2021) 61–69.
[49] X. Huang, X. Liu, Y. Zhang, J. Zhou, G. Wu, Z. Jia, Construction of $NiCeO_x$ nanosheets-skeleton cross-linked by carbon nanotubes networks for efficient electromagnetic wave absorption, J. Mater. Sci. Technol. 147 (2022) 16–25.
[50] X.F. Zhou, Z.R. Jia, X.X. Zhang, B.B. Wang, W. Wu, X.H. Liu, B.H. Xu, G.L. Wu, Controllable synthesis of Ni/NiO@porous carbon hybrid composites towards remarkable electromagnetic wave absorption and wide absorption bandwidth, J. Mater. Sci. Technol. 87 (2021) 120–132.
[51] X. Cao, D. Lan, Y. Zhang, Z. Jia, G. Wu, P. Yin, Construction of three-dimensional conductive network and heterogeneous interfaces via different ratio for tunable microwave absorption, Adv. Compos. Hybrid Mater. 6 (2023) 187.
[52] H.L. Lv, Z.H. Yang, B. Liu, G.L. Wu, Z.C. Lou, B. Fei, R.B. Wu, A flexible electromagnetic wave-electricity harvester, Nat. Commun. 12 (2021) 834.
[53] Y. Xing, Y. Cai, Z. Yan, B. Zhao, Y. Huang, W. Pan, Core-shell LaOCl/$LaFeO_3$ nanofibers with matched impedance for high-efficiency electromagnetic wave absorption, Sci. China Mater. 66 (2022) 1587–1596.
[54] C.X. Wang, B.B. Wang, X. Cao, J.W. Zhao, L. Chen, L.G. Shan, H.N. Wang, G.L. Wu, 3D flower-like Co-based oxide composites with excellent wideband electromagnetic microwave absorption, Compos. Part B Eng. 205 (2021) 108529.
[55] L. Kong, S. Zhang, Y. Liu, H. Wu, X. Fan, Y. Cao, J. Huang, Hierarchical architecture bioinspired CNTs/CNF electromagnetic wave absorbing materials, Carbon 207 (2019) 198–206.

[56] D. Mandal, K. Mandal, Enhancement of electromagnetic wave absorption in $MnFe_2O_4$ nano-hollow spheres, J. Appl. Phys. 129 (2021) 074902.
[57] F. Zhang, W. Cui, B.B. Wang, B.H. Xu, X.H. Liu, X.H. Liu, Z.R. Jia, G.L. Wu, Morphology-control synthesis of polyaniline decorative porous carbon with remarkable electromagnetic wave absorption capabilities, Compos. Part B Eng. 204 (2021) 108491.
[58] A. Xie, K. Zhang, M. Sun, Y. Xia, F. Wu, Facile growth of coaxial Ag@polypyrrole nanowires for highly tunable electromagnetic waves absorption, Mater. Des. 154 (2018) 192–202.
[59] Z.R. Jia, M.Y. Kong, B.W. Yu, Y.Z. Ma, J.Y. Pan, G.L. Wu, Tunable Co/ZnO/C@MWCNTs based on carbon nanotube-coated MOF with excellent microwave absorption properties, J. Mater. Sci. Technol. 127 (2022) 153–163.
[60] T.Q. Hou, Z.R. Jia, Y.H. Dong, X.H. Liu, G.L. Wu, Layered 3D structure derived from MXene/magnetic carbon nanotubes for ultra-broadband electromagnetic wave absorption, Chem. Eng. J. 431 (2022) 133919.
[61] J. Qiao, X. Zhang, C. Liu, Z. Wang, W. Liu, F. Wang, J. Liu, High-permittivity Sb_2S_3 single-crystal nanorods as a brand-new choice for electromagnetic wave absorption, Sci. China Mater. 64 (2021) 1733–1741.
[62] J.K. Liu, Z.R. Jia, Y.H. Dong, J.J. Li, X.L. Cao, G.L. Wu, Structural engineering and compositional manipulation for high-efficiency electromagnetic microwave absorption, Mater. Today Phys. 27 (2022) 100801.
[63] M. Chang, Q.Y. Li, Z.R. Jia, W.R. Zhao, G.L. Wu, Tuning microwave absorption properties of Ti3C2Tx MXene-based materials: component optimization and structure modulation, J. Mater. Sci. Technol. 148 (2023) 150–170.
[64] P. Bian, B. Zhan, P. Gao, Q. Yu, Y. Yang, L. Hong, W. Zhang, Investigation on the electromagnetic wave absorption properties of foamed cement-based materials, Constr. Build. Mater. 364 (2022) 129903.
[65] S. Qian, G. Liu, M. Yan, C. Wu, Lightweight, self-cleaning and refractory FeCo@MoS_2 PVA aerogels: from electromagnetic wave-assisted synthesis to flexible electromagnetic wave absorption, Rare Met. 42 (2022) 1294–1305.
[66] S.J. Zhang, Z.R. Jia, B. Cheng, Z.W. Zhao, F. Lu, G.L. Wu, Recent progress of perovskite oxides and their hybrids for electromagnetic wave absorption: a mini-review, Adv. Compos. Hybrid Mater. 5 (2022) 2440–2460.
[67] X. Tang, Z. Liao, H. Shi, R. Wang, J. Yue, X. Chen, $MoSe_2$ nanosheets decorated Co/C fibrous composite towards high efficiency electromagnetic wave absorption, Compos. A Appl. Sci. Manuf. 163 (2022) 107169.
[68] Y. Liu, X.F. Zhou, Z.R. Jia, H.J. Wu, G.L. Wu, Oxygen vacancy-induced dielectric polarization prevails in the electromagnetic wave-absorbing mechanism for Mn-based MOFs-derived composites, Adv. Funct. Mater. 32 (2022) 2204499.
[69] H.L. Lv, Y.X. Yao, S.C. Li, G.L. Wu, B. Zhao, X.D. Zhou, R.L. Dupont, U.I. Kara, Y. M. Zhou, S.B. Xi, B. Liu, R.C. Che, J.C. Zhang, H.B. Xu, S. Adera, R.B. Wu, X. G. Wang, Staggered circular nanoporous graphene converts electromagnetic waves into electricity, Nat. Commun. 14 (2023) 1982.
[70] Z. Wang, Z. Wang, M. Ning, Electromagnetic wave absorption performance of $NiCo_2X_4$ (X = O, S, Se, Te) spinel structures, Constr. Build. Mater. 259 (2020) 119863.
[71] S.J. Zhang, B. Cheng, Z.R. Jia, Z.W. Zhao, X.T. Jin, Z.H. Zhao, G.L. Wu, The art of framework construction: hollow-structured materials toward high-efficiency electromagnetic wave absorption, Adv. Compos. Hybrid Mater. 5 (2022) 1658–1698.
[72] L.F. Sun, Q.Q. Zhu, Z.R. Jia, Z.Q. Guo, W.R. Zhao, G.L. Wu, CrN attached multi-component carbon nanotube composites with superior electromagnetic wave absorption performance, Carbon 208 (2023) 1–9.
[73] X. Zhou, Z. Jia, X. Zhang, B. Wang, X. Liu, B. Xv, L. Bi, G. Wu, Electromagnetic wave absorption performance of $NiCo_2X_4$ (X = O, S, Se, Te) spinel structures, Chem. Eng. J. 420 (2021) 129907.
[74] C.H. Sun, Z.R. Jia, S. Xu, D.Q. Hu, C.H. Zhang, G.L. Wu, Synergistic regulation of dielectric-magnetic dual-loss and triple heterointerface polarization via magnetic MXene for high-performance electromagnetic wave absorption, J. Mater. Sci. Technol. 20 (2022) 128–137.
[75] J. Luo, Y. Wang, Z. Gu, W. Wang, D. Yu, Anisotropic, multifunctional and lightweight CNTs@$CoFe_2O_4$/polyimide aerogels for high efficient electromagnetic wave absorption and thermal insulation, Chem. Eng. J. 442 (2022) 136388.
[76] X.L. Cao, D.Q. Hu, G.L. Wu, Z.R. Jia, Synergistic construction of three-dimensional conductive network and double heterointerface polarization via magnetic FeNi for broadband microwave absorption, Adv. Compos. Hybrid Mater. 5 (2022) 1030–1043.
[77] Q. Han, S. Wang, X. Cheng, X. Du, H. Wang, Z. Du, Self-healing polyurethane coating based on porous carbon/Ni hybrid composites for electromagnetic wave absorption, Compos. A Appl. Sci. Manuf. 175 (2023) 107830.
[78] C.X. Wang, Z.R. Jia, S.Q. He, J.X. Zhou, S. Zhang, M.L. Tian, B.B. Wang, G.L. Wu, Metal-organic framework-derived CoSn/NC nanocubes as absorbers for electromagnetic wave attenuation, J. Mater. Sci. Technol. 108 (2022) 236–243.
[79] Z.R. Jia, X.Y. Zhang, Z. Gu, G.L. Wu, MOF-derived Ni-Co bimetal/porous carbon composites as electromagnetic wave absorber, Adv. Compos. Hybrid Mater. 6 (2023) 28.
[80] C. Ma, W. Ma, T. Wang, F. Ma, X. Xiao, C. Feng, W. Wang, An MXene coating with electromagnetic wave absorbing performance, Inorg. Chem. Commun. 151 (2023) 110565.
[81] Y. Liu, X.H. Liu, X.Y. E, B.B. Wang, Z.R. Jia, Q.G. Chi, G.L. Wu, Synthesis of Mn_xO_y@C hybrid composites for optimal electromagnetic wave absorption capacity and wideband absorption, J. Mater. Sci. Technol. 103 (2022) 157–164.